EPJ B
Condensed Matter and Complex Systems
EPJ.org
your physics journal

Eur. Phys. J. B (2013) 86: 271 DOI: 10.1140/epjb/e2013-30801-5

Interplay between spin-crossover and magnetic interactions in a BEG model

T.D. Oke, F. Hontinfinde and K. Boukheddaden

edp sciences
Società Italiana di Fisica
Springer

Eur. Phys. J. B (2013) 86: 271
DOI: 10.1140/epjb/e2013-30801-5

THE EUROPEAN PHYSICAL JOURNAL B

Regular Article

Interplay between spin-crossover and magnetic interactions in a BEG model

T.D. Oke[1], F. Hontinfinde[1,a], and K. Boukheddaden[2]

[1] Département de Physique (FAST) et Institut des Mathématiques et de Sciences Physiques (IMSP), Université d'Abomey-Calavi, 01 BP 613, Porto-Novo, Benin
[2] Groupe d'Etudes de la matière condensée, Université de Versailles/St. Quentin en Yvelines-CNRS, 45 Avenue des Etats Unis, 78035 Versailles Cedex, France

Received 3 September 2012 / Received in final form 2nd March 2013
Published online 17 June 2013 –

Abstract. A two-dimensional Blume-Emery-Griffiths spin-1 model with spin-phonon interaction is introduced to investigate the thermodynamic properties of Prussian Blue Analogs and Spin-crossover materials. The quadrupolar interaction parameter is assumed to depend on the temperature in the form $K = \alpha k_B T$ while the crystal-field depends both on the ligand-field strength and the degeneracy ratio between high spin (HS) and low spin (LS) states as in some previous works. The model is solved by means of two statistical-mechanical methods: kinetic Monte Carlo simulations and corrective effective field theory calculations. Our calculations indicate that by tuning α, the spin-crossover transition changes to a sharp first order transition where the HS fraction, n_{HS} changes discontinuously. Second order transitions are observed in the presence of magnetic ordering when the nearest-neighbor coupling constant J exceeds some critical value J_c which depends on α and other model parameters. Below J_c, simple spin-transition occurs at an equilibrium temperature T_{eq} that is very sensitive to the values of the degenaracy ratio and the ligand-field. Competition between model parameters lead to interesting phase diagrams. Some of them are displayed for varying values of the coupling J and also in the specific case where J and K are of the same order of magnitude. Thermal hysteresis loops have been calculated by Monte Carlo simulations and also by using the self-consistent equations in the case of long-lived metastable states showing strong dependence on model parameters.

1 Introduction

Spin-crossover (SC) compounds are materials with fascinating properties that attracted much attention from physicists and chemists over the few past years [1–7]. The evolution of magnetic and transport properties of these materials with the temperature has been explored by several authors [8,9] but the details of the spin-state transition that occurs are still a matter of debate. It is now well-established that these materials constitute good examples of bistable solids [10]. Due to this character, they are potential candidates for information storage devices. Since their discovery 70 years ago by Cambi and Gagnasso [11], the SC transition phenomenon has been observed in numerous compounds of Fe^{II} ($3d^6$), Fe^{III} ($3d^5$) and C_o^{II} ($3d^7$), either in solid state [12] or in solution [13], and more recently in nanocrystals [14,15]. The change of the system thermal energy during the spin-state transition leads to both electronic and structural changes, often observed as a colour and/or magnetic moment change [16]. SC materials give also rise to a type of molecular magnetism where the spin state and the magnetic moment of the central d block ion can be changed or controlled by external stimuli, such as light, magnetic and electric fields, pressure, etc. [17,18]. For this phenomenon to occur, the involved metal ion needs to be 6-coordinated with the outer electronic configuration of d^4 to d^7. The most common example is Fe^{II} (mainly observed in octahedral coordination complexes) where the outer electronic configuration is $3d^6$, and the electrons can occupy all the lower t_{2g} level ($S = 0$), which corresponds to the low-spin (LS) state or they can occupy both t_{2g} and eg levels ($S = 2$) corresponding to the high-spin (HS) state [16,19]. The spin state of the Fe^{II} ion changes then from diamagnetic ($S = 0$) in the LS state, to paramagnetic ($S = 2$) in the HS state. Thus, the transition takes place due to the competition between the splitting energy (between the t_{2g} and eg orbitals) and the spin pairing energy. The occupation of the antibonding orbitals, eg, in the HS spin state, results in a weakening of the iron-nitrogen bonds leading to an increase of the molecular volume. Therefore, the difference of molecular volumes in the two spin states results in strong elastic interactions [20], of long-range nature, since they are mediated by the lattice. If they are strong enough, they can lead to first-order transitions, accompanied by wide hysteresis

[a] e-mail: fhontinfinde@yahoo.fr

loops, such as thermally or a pressure-induced hysteresis obtained at the vicinity of first order spin transitions [21].

In the present work, we extend the usual problem of SC transition to include the new degree of freedom of possible magnetic interactions between the HS species. To avoid similar descriptions as in reference [22], we have considered an explicit thermal dependence of the "elastic interactions" depicted by the coupling K. It is taken here to depend linearly on the absolute temperature T in view to account in a simple way for the spin-phonon contributions to SC materials' properties [23,24]. Although introduced in an ad hoc way in the previous version (Ref. [22]), we now give the physical reasons of this dependence as well as the condition of its validity. The model is of a Blume-Emery-Griffiths (BEG) type and is defined on a square lattice with periodic boundary conditions. The two-dimensional model is much more adapted for the theoretical developments than for the SC materials themselves, although most of the models designed for the SC transition are of 1D or 2D character. SC materials however, may have in some cases strong specific 2D natures (this is the case for triazole ligands), but the architectures can be also spatially extended and form 3D supramolecular systems. It is very difficult to catch theoretically this nature of the molecular solid. The crystal-field strength depends on the absolute temperature, T, of the system, the degeneracy ratio between LS and HS states and the ligand-field. The model is investigated by means of two statistical-mechanical methods, namely the corrective effective field theory (CEFT) approach due to Kaneyoshi and Tamura [25] and Kinetic Monte Carlo (KMC) simulations with the algorithm developed by Bortz, Kalos and Lebowitz (BKL) [26,27]. Spin-flip dynamics are governed by Glauber kinetics [28], instead of the usual Arrhenius dynamics used in previous works. The equilibrium temperature obtained by both methods are compared to the one derived analytically by mapping the model onto a two-state Ising model known as the WP model [29] in the case where magnetic ordering is irrelevant and a remarkable agreement has been observed. Finite-temperature phase diagrams in the presence of magnetic ordering are presented and show a strong sensitivity of the spin transition temperature to values of model parameters.

In Section 2, we describe the model Hamiltonian while in Section 3, the CEFT formalism is revisited. Section 4 deals with the Monte Carlo simulation algorithm. In Section 5, we discuss different results. Section 6 is devoted to conclusions.

2 The model Hamiltonian

A three states BEG-type Hamiltonian with spin variables $S = 0, \pm 1$ is chosen to describe the spin-crossover phenomenon. It reads:

$$H = -J \sum_{\langle i,j \rangle} S_i S_j - K \sum_{\langle i,j \rangle} S_i^2 S_j^2 + D \sum_i S_i^2, \qquad (1)$$

where J denotes the nearest-neighbor exchange coupling. The parameters K and D are the quadrupolar interaction and the lattice anisotropy constants, respectively. In the model, these parameters are at least temperature-dependent (see below). The first sum runs over magnetic interacting nearest-neighbors. The second one represents the biquadratic isotropic exchange interactions which should be considered for a high-spin system ($S \geq 1$) [30]. Adler gave a discussion of this term through an extensive review [31] of experimental results which established its importance in a variety of compounds. The third term is a single ion anisotropy energy due to cristalline field. The crystal-field also plays an important role for materials consisting of spins with values larger than 1/2. If the crystal-field is strong enough, the energy difference between the splitted levels is large. In that case, it is energetically more favorable to fill low level orbitals and pair them up with opposite spins before starting to fill higher energy levels. This results in no addition to the total spin and to a low spin state.

Originally, Hamiltonian (1) has been introduced to describe the thermodynamic properties of He^3-He^4 mixtures [32]. Later, using an extended version to lattice gas model, Sivadiere and Lazerowitch [33] have studied condensation and phase separation in binary fluids.

In the model, $S = 0$ denotes the nonmagnetic state while $S = \pm 1$ corresponds to the magnetic state. Degeneracies of nonmagnetic and magnetic states are different. Let us first point out that the spin states are fictitious spin states and not true spins. The spin value $S = 0$ is affected to the LS state (which has a true total magnetic spin $S = 0$) and the spins $S = \pm 1$ are associated with the HS state (which has a true total spin $S = 2$). In the problem, the degeneracy of the true spin is included in the ratio of the effective degeneracies between the HS and the LS states (see Appendix A). Let us denote by g_0 and $g_+ = g_-$ the degeneracies of states $S = 0$ and $S = \pm 1$, respectively, and by g the degeneracy ratio g_+/g_0. The ratio g is related to the molar entropy change due to total spin conversion. Generally, g depends on the temperature through the phonon density of the lattice. Here, it is taken as a constant. The contribution of the magnetic coupling J is negligible in the case of SC solids and very minor in the case of PBA [22]. However, very recent experimental data obtained on the bimetallic coordination polymeric compound, $Fe_2(Nb(CN)_8)$-(4-pyridinealdoxime)$_8$-$2H_2O$ [34] have shown the existence of an intermediate spin state which exhibits a long-range ferromagnetic order between the Fe and Nb spins, as opposed to the long-range antiferro-magnetic order operating between the Fe (HS) and Nb spins. The results show also a possible temperature and pressure control of the switching of the long-range magnetic order.

A realistic model that describes SC solids may consider the spin-phonon contribution to physical properties of the system. So coupling constants may depend on lattice elastic constants and/or the absolute temperature. The main interaction between spin-crossover units which generates the first-order transitions between the

LS and the HS states is elastic in nature. It originates from the volume change accompanying the spin state change at the molecular level. The volume change delocalizes the phenomenon over the lattice, leading to the formation of long-range order, and hence to the appearance of the HS state at high temperature. This is one of the fundamental aspects of the spin-crossover transition. This interaction is represented in our relation (1) by the coupling parameter K. In a much more sophisticated model, the neighboring spins S_i and S_j are connected via springs, and the interaction between them can be written as $\sum_{\langle i,j\rangle} K_0 S_i^2 S_j^2 (u_j - u_i)^2$, where u_i and u_j are the local distortions of sites i and j. It is a formidable task to exactly solve Hamiltonians of this type beyond classical statistical mechanics, although some approximate methods allow some interesting developments. In the local equilibrium approach, we assume that the phonon bath equilibrates very rapidly compared to the electronic system, which is coupled with the internal distortion of the molecule. As a result, the quadratic displacement $(u_j - u_i)^2$ and the phonon energy are constrained to follow adiabatically the spin quantities. Therefore, we replace the quadratic displacement $(u_j - u_i)^2$ by its statistical average, $\overline{(u_j - u_i)^2}$. In classical mechanics, this quantity depends linearly on temperature, $\overline{(u_j - u_i)^2} \propto k_B T$, which leads to the contribution $\sum_{\langle i,j\rangle} \alpha k_B T S_i^2 S_j^2$. Let us now discuss of the validity of this linear dependence in temperature. From the experimental point of view, the transition temperatures in spin crossover solids take place in the interval 200–300 K, i.e. at quite high temperature. In this temperature interval, the classical mechanics behavior can be reasonably admitted as valid. To our best knowledge, there is only one case of spin-crossover transition taking place around 50 K [35]. It concerns a system of $Mn^{III}(Mn(taa))$ in which, however, the spin transition is coupled with Jahn-Teller distortion of the Mn ion.

In the following, we take $K = \alpha k_B T$. Despite this simplification, the resulting Hamiltonian enables one to describe most of the properties of SC solids (see below). The crystal-field interaction parameter is written in the form (see Ref. [20] and references therein): $D = \Delta - k_B T \ln(g)$ due to the existence of an entropy difference between HS and LS states of the system. Δ stands for the ligand-field energy.

Two numerical techniques are considered below to investigate the model: the CEFT method due to Kaneyoshi and collaborators [25,36] and the KMC simulations technique with the Bortz, Kalos and Lebowitz (BKL) algorithm [26,27].

3 The CEFT formalism revisited

In this section, we briefly describe the CEFT technique that we first consider to study the present model. It uses exact Ising spin identities and the Honmura-Kaneyoshi differential operator [37,38] to generate expressions of the magnetization, the quadrupolar moment and correlation functions. For the BEG model, these identities are [37]:

$$\langle f_i s_i \rangle = \left\langle f_i \prod_\delta P_i(s_{i+\delta}, (s_{i+\delta})^2, \nabla_x, \nabla_y) \right\rangle f(x,y)_{/\substack{x=0\\y=0}}, \tag{2}$$

$$\left\langle f_i s_i^2 \right\rangle = \left\langle f_i \prod_\delta P_i(s_{i+\delta}, (s_{i+\delta})^2, \nabla_x, \nabla_y) \right\rangle g(x,y)_{/\substack{x=0\\y=0}}, \tag{3}$$

where x and y denote the nearest neighbors' interaction fields: $x = J\sum_j s_j$ and $y = K\sum_j s_j^2$ that act on site i; $\nabla_\mu = \partial/\partial\mu$ ($\mu = x, y$) are the two differential operators and f_i represents any functions of the Ising variables that are not functions of the site i. The operator function $P_i(s_{i+\delta}, (s_{i+\delta})^2, \nabla_x, \nabla_y)$ is defined by:

$$P_i(s_{i+\delta}, (s_{i+\delta})^2, \nabla_x, \nabla_y) = e^{K(s_{i+\delta})^2 \nabla_y} e^{J s_{i+\delta} \nabla_x}. \tag{4}$$

Identities (2) and (3) may be treated by using Van der Waerden type identity [38]:

$$e^{\delta s_i} e^{\delta' s_i^2} = 1 + s_i e^{\delta'} \sinh(\delta) + (s_i)^2 e^{\delta'} \cosh(\delta) - (s_i)^2 \tag{5}$$

from which equation (4) reduces to:

$$P_i(s_{i+\delta}, (s_{i+\delta})^2, \nabla_x, \nabla_y) = 1 + s_{i+\delta} e^{K\nabla_y} \sinh(J\nabla_x) + (s_{i+\delta})^2 e^{K\nabla_y} \cosh(J\nabla_x) - (s_{i+\delta})^2. \tag{6}$$

The functions $f(x,y)$ and $g(x,y)$ are defined by:

$$f(x,y) = \frac{2\sinh(\beta x) e^{\beta y}}{2\cosh(\beta x) e^{\beta y} + e^{-\beta D}}, \tag{7}$$

$$g(x,y) = \frac{2\cosh(\beta x) e^{\beta y}}{2\cosh(\beta x) e^{\beta y} + e^{-\beta D}}, \tag{8}$$

where $\beta = 1/k_B T$.

On the other hand, Kaneyoshi and Tamura [25,37] and Honmura [36] have refined a decoupling approximation named Zernike's approximation [39], by introducing two new correlated effective-field parameters λ and μ [38]:

$$\begin{aligned} s_{i+\delta} &= \langle s_{i+\delta} \rangle + \lambda(s_i - \langle s_i \rangle), \\ (s_{i+\delta})^2 &= \langle (s_{i+\delta})^2 \rangle + \mu \left[(s_i)^2 - \langle (s_i)^2 \rangle \right]. \end{aligned} \tag{9}$$

As shown in relations (9) of reference [37], $\mu = \lambda$. Substituting (9) into (2), (3) and (6) and setting $f_i = 1$ as in reference [40], equations (2) and (3) can be written as:

$$\left\langle \prod_\delta P_i(s_{i+\delta}, (s_{i+\delta})^2, \nabla_x, \nabla_y) \right\rangle = \left\langle \Big[(1-\lambda) P(m, q, \nabla_x, \nabla_y) + \lambda e^{J s_i \nabla_x} e^{K s_i^2 \nabla_y} \Big]^z \right\rangle, \tag{10}$$

where

$$P(m, q, \nabla_x, \nabla_y) = 1 + m e^{K\nabla_y} \sinh(J\nabla_x) + q e^{K\nabla_y} \cosh(J\nabla_x) - q \tag{11}$$

and z the coordination number.

Functions $f(x,y)$ and $g(x,y)$ in relations (7) and (8) satisfy the following conditions:

$$f(x,y) = -f(-x,y), \quad g(x,y) = g(-x,y), \tag{12}$$

and the mathematical relation for any function $F(x)$:

$$e^{\delta\nabla_x} F(x) = F(x+\delta). \tag{13}$$

Expressions of the magnetization, the quadrupolar moment and correlation functions for the spin-1 BEG model may be deduced from the following self-consistent equations [40]:

$$\begin{aligned} m &= A_1(q)m + A_2(q)m^3 \\ q &= B_1(q) + B_2(q)m^2 + B_3(q)m^4 \\ \langle s_i s_{i+\delta}\rangle &= C_1(q) + C_2(q)m^2 + C_3(q)m^4, \end{aligned} \tag{14}$$

where, the functions $A_i(q)(i = 1,2)$, $B_j(q)$ and $C_j(q)$ $(j = 1,\ldots,3)$ are defined in the Appendices B and C. The phase diagram of the system for a given coordination number z is obtained by studying the thermal variations of the order parameters. By recursively solving the previous equations, (m,q) converges to the fixed point (m_t,q_t), which corresponds to the stability point of the system.

The HS fraction (n_{HS}) corresponds to the quadrupolar moment. Two quantities are estimated in order to determine magnetic transitions in the model. These are, the magnetic susceptibility calculated using the following fluctuation expression [41]:

$$\chi = (\langle s_i s_{i+\delta}\rangle - \langle s_i\rangle^2)/T \tag{15}$$

and the fourth-order cumulant U given by:

$$U = 1 - \frac{\langle s_i\rangle^4}{3\langle s_i s_{i+\delta}\rangle^2}. \tag{16}$$

4 Kinetic Monte Carlo simulation

Monte Carlo simulations are numerical experiments that have been proven efficient in studying a wide variety of physical systems ranging from elementary particle systems to those in astronomy. Here, we use the n-fold algorithm developped by BKL [26,27] to investigate the model properties. In the simulation procedure, an initial configuration σ (of linear size L) of the system is chosen. Then one calculates the total number of possible spin-flip processes that lead to another configuration σ', say N. Let us denote by $w(\sigma \to \sigma')$ the transition probability from σ to σ'. By using the Glauber spin-flip dynamics, w reads [28]:

$$w(\sigma,\sigma') = \frac{1}{1+e^{\beta\Delta E}}, \tag{17}$$

where ΔE denotes the change in the system energy associated to the spin-flip move. Then, one calculates the total evolution rate $Q(\sigma)$ of σ by considering all possible processes:

$$Q(\sigma) = \sum_{a=1}^{N} w_a, \tag{18}$$

where a stands for the number of a possible spin-flip process. After that, two random numbers $0 \le r_1, r_2 \le 1$ are chosen to calculate the lifetime $\tau(\sigma) = -\ln(r_1)/Q(\sigma)$ of configuration σ and a random evolution rate: $\eta(\sigma) = r_2 Q(\sigma)$. The process numbered b such that the partial sum

$$\sum_{a=1}^{b} w_a > \eta(\sigma) \tag{19}$$

is realized with probability 1. After a suitable number n_{MC} (found to be about 4×10^3 L^2) of Monte Carlo steps, stationary values of physical quantities of interest are obtained. The total evolution time $\overline{t}$ is given by: $\overline{t} = \sum_\sigma \tau(\sigma)$, where the sum runs over all spin configurations generated up to the steady state. Different physical quantities $(m, q = n_{HS}, \chi, U)$ are calculated by a time-averaging procedure. Thus, the expression of n_{HS} reads:

$$n_{HS} = \overline{t}^{-1} L^{-2} \sum_\sigma \tau(\sigma) n(\pm)_\sigma, \tag{20}$$

where $n(\pm)_\sigma = n(+)_\sigma + n(-)_\sigma$, and $n(+)_\sigma/n(-)_\sigma$ denotes the number of up/down spins of the configuration σ. In the case of the magnetization, $n(\pm)_\sigma$ in the previous formula should be replaced by $n(+)_\sigma - n(-)_\sigma$.

5 Results and discussions

5.1 On spin-crossover materials case

The simulation algorithm is first checked through comparison of some numerical results by KMC and by the transfer matrix and finite-size scaling (TMFSS) technique [42] in the simpler case where in the BEG model, the reduced coupling parameters $D/J = 0$; $K/J = 0$. Figures 1a and 1b show KMC results averaged over 10 independent runs on the magnetization m and the fourth-order cumulant $U = 1 - \frac{\langle m^4\rangle}{3\langle m^2\rangle^2}$ for a square lattice of different sizes. Concerning the magnetization, it appears that finite-size effects are present up to size $L = 80$ since m does not vanish at the order-disorder transition. The Binder crossing point of the cumulants is determined (see Fig. 1b) using $L = 30$, $L = 40$ and $L = 60$ and one gets $T_c/J = 1.69$. Larger sizes may not substantially modify this finding. Using correlation lengths calculated by the TMFSS method on two semi-infinite systems with sizes $L = 5$ and $L = 6$, we get $T_c/J = 1.70$ (Fig. 1c), which is very close to the one obtained through KMC calculations and also in agreement with those reported in reference [42]. One can conclude that the KMC procedure seems reliable and generates some accurate results. Another check is done through Figure 1d. The high-spin fraction n_{HS} is calculated. At $T/J = 0$, this obvioulsy yields the value 1; but as the

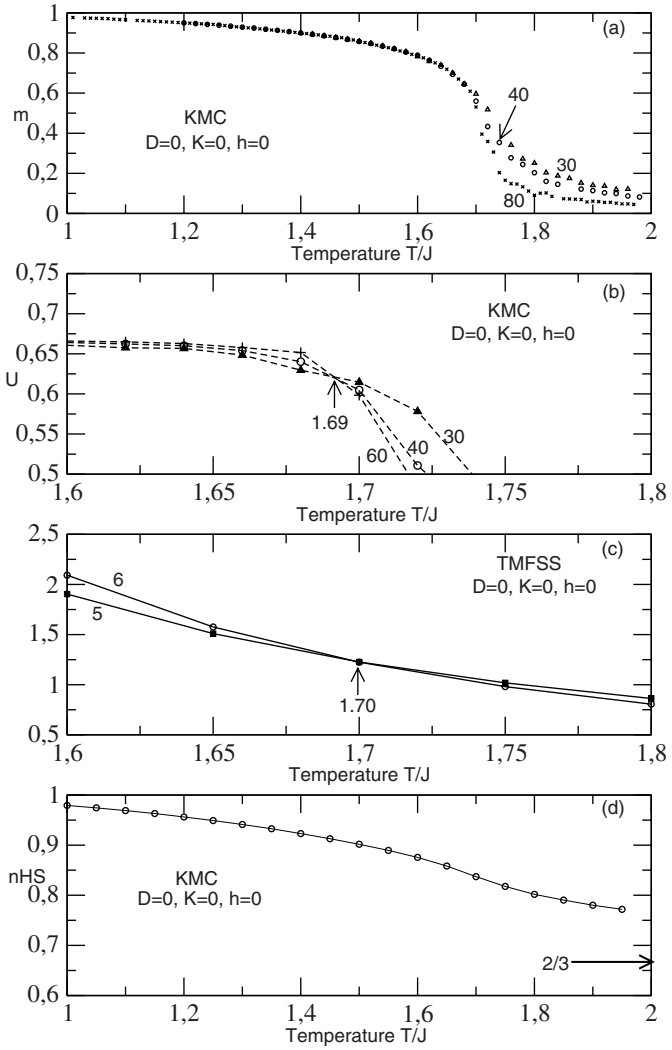

Fig. 1. Thermal behavior of the magnetization for (a) three system sizes: $L = 30; 40; 80$ in the case where only the exchange coupling constant $J \neq 0$. (b) The fourth-order cumulant for the system sizes ($L = 30$, $L = 40$ and $L = 60$), showing the Binder crossing point indicating a critical temperature $T/J = 1.69$. (c) The correlation lengths for two semi-infinite systems of sizes $L = 5$ and $L = 6$ calculated by the TMFSS method, showing a crossing point $T/J = 1.70$, corresponding to a second-order transition point. (d) The thermal behavior of the HS fraction $q = n_{HS}$, which saturates at the value 2/3 at high temperature, as a result of thermal equipopulation of HS and LS levels.

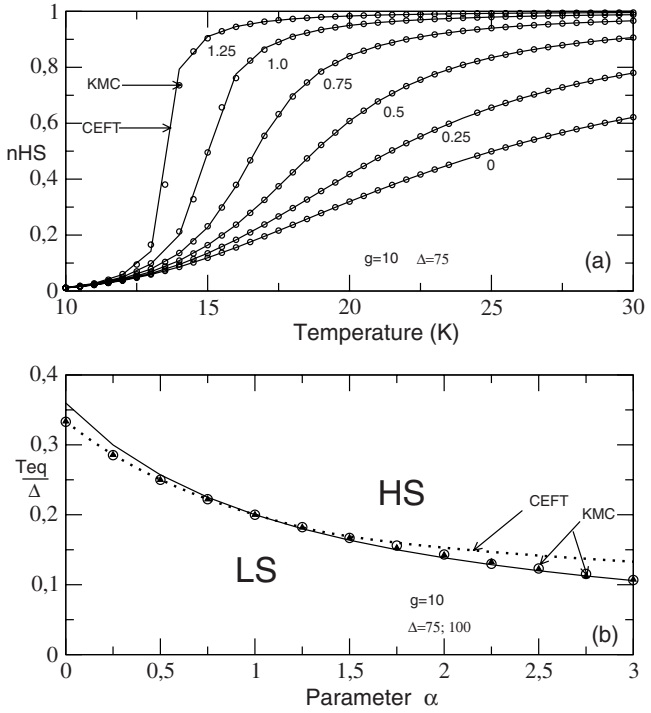

Fig. 2. Compared results by CEFT and KMC simulations on the model for increasing values of the parameter α and temperature T. (a) Thermal evolution of the HS fraction n_{HS} for KMC (open circles) and CEFT (lines) findings. (b) The α-dependence of the normalized equilibrium temperature obtained by solving the equation $n_{HS} = \frac{1}{2}$: dotted points are CEFT results; open circles and triangles correspond to results by KMC simulations for $\Delta = 75$ K and $\Delta = 100$ K, respectively. Full line is the best fitting-curve for $\Delta = 75$ K (see text). The transition becomes of first order for α exceeding some critical value $\alpha_c = 1.5$.

temperature is raised, this value decreases due to thermal fluctuations to the asymptotic value 2/3 corresponding to a disordered system where 2/3 of the lattice may be covered by spins of values ± 1 and the remaining part by spins of value 0. The high-spin fraction is found to quickly saturate with system size at fixed other parameters. Indeed, results obtained on this quantity on sizes $L = 40$ and $L = 80$ coincide up to several digits.

We now turn to the spin-crossover problem. Here, the coupling constant J which may quantify magnetic interactions among HS units is set to zero in the Hamiltonian. Thus, magnetic ordering is not expected at any temperature ($m = 0$). The quadrupolar moment ($q = \langle S^2 \rangle$), which corresponds to the high-spin fraction n_{HS} remains the key order parameter. Equations (14) have been numerically solved using $\lambda = 0$. Non-zero values of λ give approximatly the same quantitative results. The correction to the effective-field in the present model seems marginal. In Figure 2a, we display compared results by KMC (open circles) and CEFT (lines) on n_{HS} as a function of the absolute temperature for varying values of the parameter α. Agreement between results by both methods appears evident at least in the α range analyzed. For larger values of α which may correspond to the domain of high contribution of spin-phonon interaction and lattice elastic constants, some discrepancy is observed (see below). n_{HS} behaves as in several previous works: it increases and obviously tends to the value 1 at high temperature. The so-called spin transition temperature T_{eq} is defined as the temperature at which $q = n_{HS}$ is right 1/2. This transition becomes sharper and sharper as the quadrupolar parameter α increases and at large values, it is reached through a jump in the behavior of n_{HS}. Then, the spin transition occurs by a smooth conversion or through a

first order transition. As it emerges from Figure 2b, where data points are KMC results and the dotted line denotes those by CEFT, T_{eq} is very sensitive to the ligand-field strength Δ. Our calculations show that Δ stabilizes the LS state in the model since T_{eq} is shifted to higher temperature when it increases. Its reduced values Δ/T_{eq} are however independent of that strength since curves for $\Delta = 75$ K and $\Delta = 100$ K (Fig. 2b) coincide up to $\alpha = 3$. Up to $\alpha = 1.5$, the agreement between both methods appears remarkable. The KMC data suggest a behavior of T_{eq}/Δ best-fitted to the form $1/(a + b\alpha)$ (see full line in Fig. 2b). The numerically extracted constants a and b have the values 2.996 and 2, respectively. They are consistent with those obtained from an analysis of the Hamiltonian [22], which yields the exact behavior of T_{eq}/Δ with α in the absence of magnetic order. For the exact calculations, let us remark that flipping any spin does not change the Hamiltonian. Thus, it is easy to define a new operator $\sigma_i = 2S_i^2 - 1$ that has two values $(+1)$ and (-1) corresponding to $S_i = \pm 1$ and 0. In that case, the Hamiltonian reduces to the WP-like model [22,43] (with however a temperature-dependent interaction parameter) which leads to a first order transition (see Ref. [22] and references therein). By setting the effective-field in the resulting Ising Hamiltonian to 0, one gets:

$$k_B T_{eq}/\Delta = \frac{2}{2\ln(2g) + z\alpha}, \tag{21}$$

where z stands for the coordination number of lattice sites. It is straightforward to see that in the absence of the spin-flip symmetry ($J \neq 0$), the Hamiltonian becomes more complicated and it is no more possible to establish such isomorphism with the two states Ising model. Therefore, T_{eq} cannot anymore be calculated exactly. It might be possible within some approximation, e.g. in the Bethe-Peierls scheme. In Figure 2, the values $g = 10$ and $z = 4$ (square lattice) are used. The right-hand side of the previous formula doest not depend on Δ and this appears consistent with the KMC results displayed in Figures 2b and 3a. Let us remark in Figure 3a that KMC results are closer to the exact values of T_{eq} (full line) than findings by CEFT.

Above the transition lines, the system may be in HS state with magnetically disordered configurations. Below, the diamagnetic phase should prevail. Figure 3b shows the effect of g as a driving force for the spin transition. There, the HS fraction of molecules of the system is plotted against the rescaled temperature T/T_{eq} for $\alpha = 1$. Increasing the value of g sharpens the spin transition between LS and HS states and stabilizes the HS state. This effect is not observed with Δ. At $T/T_{eq} = 1$, $q = n_{HS} = 1/2$. This value is a constant that is independent of model parameters. This explains why all curves cross at $T/T_{eq} = 1$ and $n_{HS} = 1/2$. The behavior bears some resemblance with the one obtained for n_{HS} at T_{eq} and varying elastic constants $e+-$ in reference [20]. One may expect the same behavior for varying values of Δ. In fact data collapse curves are obtained in the case where g is fixed and Δ varies (see Figs. 3c and 3d). Indeed, T/T_{eq} is not a function of Δ but depends on g, α and z. When α, z and g are fixed, it should

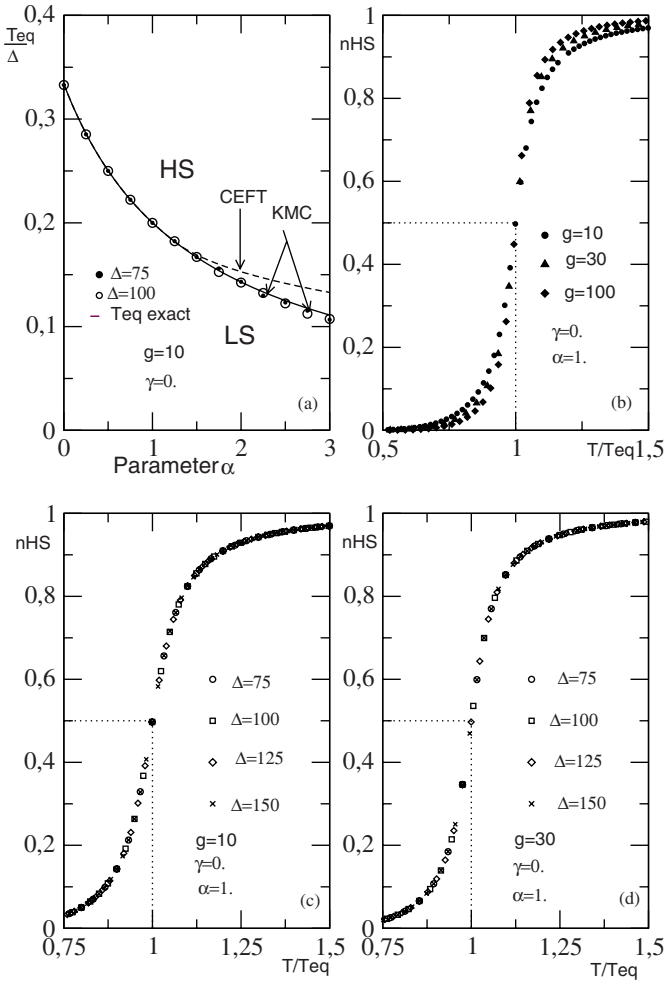

Fig. 3. (a) Finite-temperature phase diagrams obtained by three different methods: KMC simulations (full and open circles), CEFT (dashed line) and exact calculations (line; see text) for $g = 10$, $\Delta = 75$ K; $\gamma = 0$ and varying α. In (b) the influence of the degeneracy ratio, g, on the transition is shown. The curves coincide only at $T/T_{eq} = 1$ whereas in (c, d) optimal data collapse curves are got for different values of Δ at fixed values of g.

be the same at any value of Δ as shown in the figures. Up to now, the ligand-field strengths and the degeneracy ratio considered are weak. Usual values of Δ are around 475 K; this means that T_{eq} may be higher than those previously reported, e.g. in Figure 2. For $\Delta = 450$ K and $g = 100$, we get: $T_{eq} = 39.83$ K for $\alpha = 3.0$; $T_{eq} = 54.23$ K for $\alpha = 1.5$; $T_{eq} = 61.66$ K for $\alpha = 1.0$; $T_{eq} = 71.45$ K for $\alpha = 0.5$.

According to reference [22], the order parameter in the absence of magnetic ordering should present two types of behavior within the mean-field approach depending on model coupling constants: a first-order spin-crossover transition with a hysteresis loop or a smooth conversion between the LS and HS states. In the present model, we also observe hysteresis loops at the vicinity of the first-order spin transition. Its existence, shape and position are strongly sensitive to the variation of model

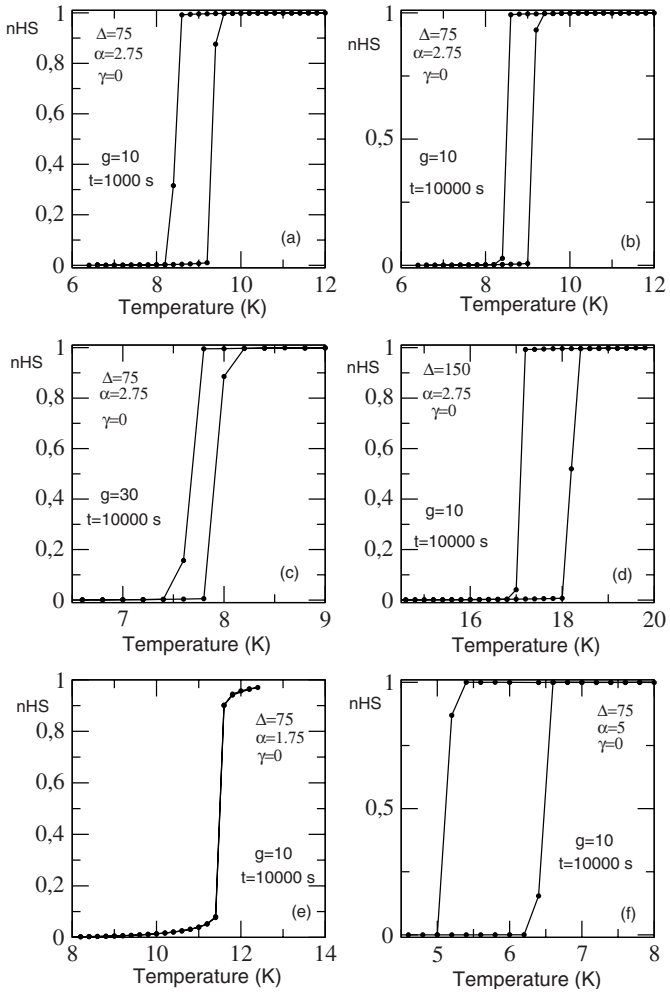

Fig. 4. Thermal hysteresis loops of the HS fraction obtained from KMC simulations for varying values of model parameters in the absence of magnetic ordering ($\gamma = 0$).

parameters, real simulation or duration time and temperature steps. They should appear when T_{eq} is smaller than the critical temperature of the corresponding Ising model [22]. Here, we raised the temperature sequentially from $T = 5$ K to $T = 20$ K with a temperature step $\Delta T = 0.2$ K and then reduced to $T = 5$ K again. Different results obtained for selected values of model parameters are displayed in Figure 4. From panel (a) to panel (b), the duration time is increased and consequently, the area of the hysteresis loop decreases while its center is conserved. It then appears clear that for $t \to \infty$, upward and backward processes should be superimposed at each temperature leading to a unique curve with a first order transition jump at the equilibrium temperature. An increase of g/Δ (panels c and d) shifts the hysteresis loop to high/low temperatures as already observed for the spin transition temperature in our preliminary results. Panels (e) and (f) show the influence of α on the thermal hysteresis loop. At large values of α, the loop's area is large with a T_{eq} shifted to low temperatures. On the contrary, for small values of α, i.e. small values of the coupling parameter K, the loop is almost inexistent (panel e). One may expect it to disappear at very low values where only smooth conversion of LS spins to HS spins is observed (see Fig. 2a). These results suggest the existence of a critical value of α from which the SC transition becomes of first-order.

The effect of magnetic interaction on the hysteresis loop will be studied in the next section.

It is worthwhile to recall the reader that the spin-crossover transition arises from electronic and distortion degrees of freedom. In most of the cases, the orbital moment is quenched. This implies a charge redistribution accompanied with a molecular volume change when the molecule goes from a total spin $S = 0$ (in the LS state) to a total spin $S = 2$ in the HS spin state, which appears at high temperature. Large changes in vibrational degrees of freedom accompany this electronic transition, and then play also a crucial role, in particular in enhancing the entropy of the high-spin state. Therefore, the spin-crossover transition is an electro-vibrational phenomenon. Thus, the name spin transition is somehow not so appropriate because it masks the important role of the molecular distortion in the physical mechanism of this transition.

5.2 The general spin-crossover model

Here, $J \neq 0$: HS thermally created units interact magnetically. We first study the model in the specific cases where couplings J and K are of the same order of magnitude, say $J/K = \gamma$ taken as a constant. Thus, J behaves linearly with the temperature. Figure 5a displays the behaviors of the HS fraction calculated by CEFT with temperature for selected values of α, g and Δ for γ varying from 0.4 to 1. One remarks that the magnetic interaction stabilizes the HS state and sharpens the spin transition. In Figure 5b, corresponding nearest-neighbor correlation functions $C = \langle s_i s_{i+\delta} \rangle$ are plotted. They show two trends: spins are strongly correlated for $\gamma > 0.7$ with large values of n_{HS} whereas for γ below 0.7, the opposite holds. It is clear that between these two visible trends, an order-disorder transition occurs. One observes that at $\alpha = 0.5$ and γ of the order of 0.6, the only one transition that can be seen is that of a smooth spin transition during the variation of the HS fraction. From $\gamma = 0.8$, a jump appears in the behavior of the correlation function, which means that another kind of transition occurs. This statement is strengthened by the analysis of the behaviors of the magnetic susceptibility χ and the fourth-order cumulant U in this range of parameters (see panels c and d). Indeed, a peak arises in χ around $\gamma \simeq 0.7$ and U shows a transition point around 32 K. For $\gamma = 0.66$, the transition is observed at $T_c = 68.98$ K. For values of γ less than 0.66, one remarks that the cumulant $U \simeq 1$ at any temperature and this is consistent with the phase diagram displayed in Figure 6b (see below). Thus, for $\gamma < 0.66$, T_c does not exist. Therefore, the transition between the two trends of the correlation function in Figure 5b occurs right at $\gamma = 0.66$. One sees also that the transition becomes sharper and sharper as γ increases at fixed values of α (see Fig. 5c).

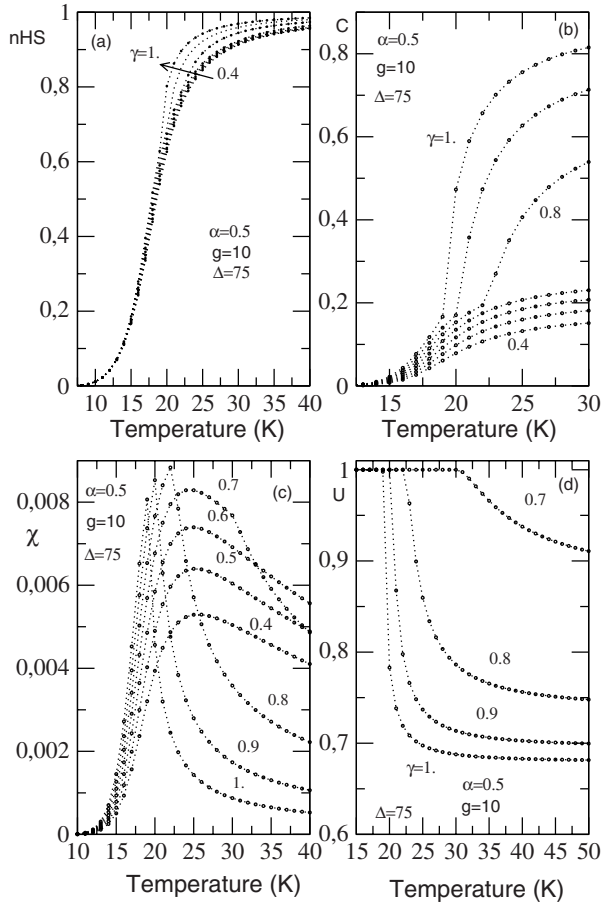

Fig. 5. Temperature- and γ-dependence of some physical quantities calculated by CEFT: (a) the HS fraction n_{HS}; (b) the nearest-neighbor correlation function C, (c) the magnetic susceptibility χ and (d) the fourth-order cumulant U for $\alpha = 0.5$, $g = 10$ and $\Delta = 75$ K.

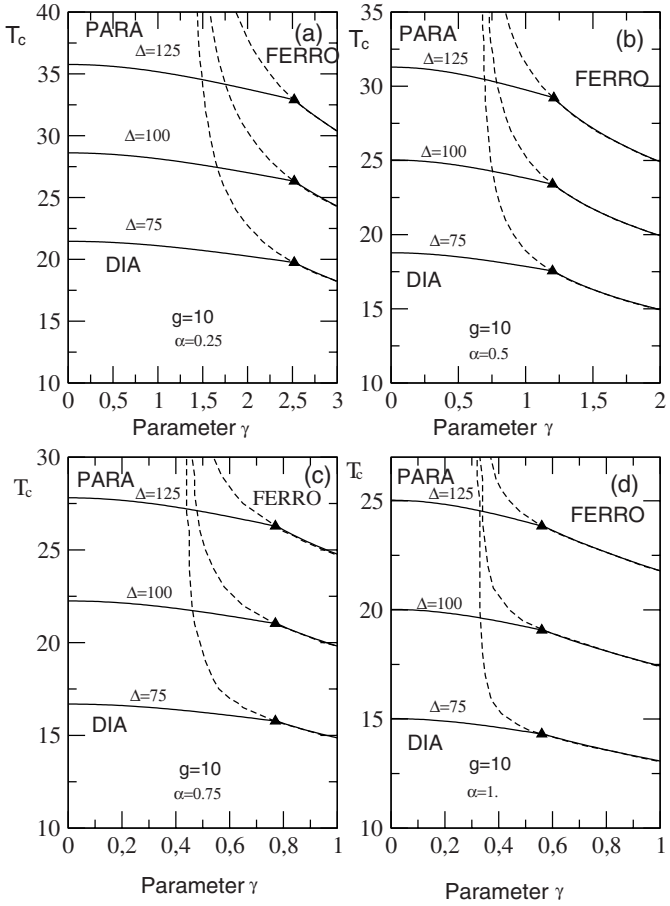

Fig. 6. Finite-temperature phase diagrams obtained by CEFT in the plane (γ, T) for varying model parameters in the presence of magnetic interaction. Full triangles denote tricritical points (TCP). Dashed lines are magnetic second-order transition lines. Full transition lines have first-order character at the right-hand side of TCP while at the left-hand side, they characterize the smooth spin transition in SC solids.

The phase diagrams in Figures 6 and 7 are obtained using relation $n_{HS} = 1/2$ to find the equilibrium temperature T_{eq} during the spin-transition and by determining the temperature at which $A_1(q) = a = 1$ in equations (14). The last condition yields the second order ferro-para transition line. At the vicinity of this transition, the magnetization should behave as:

$$m^2 = \frac{1-a}{b}, \tag{22}$$

where $b = A_2(q)$. When the right-hand side of this relation is negative, one gets a first-order transition. The tricritical point (γ_α^T) corresponds to the case $a = 1$ with jumps in the behaviors of m and q. In Figures 6 and 7, dashed lines are second-order transition lines. At each critical point, both order parameters vanish continuously. Full lines correspond to the spin-transition obtained through the relation $n_{HS} = 1/2$. The two curves coincide for $\gamma \geq \gamma_\alpha^T$ where one has, according to the sign of m^2, a first order transition. One interesting result is that γ_α^T is independent of Δ and g. For increasing values of α, γ_α^T tends to zero. Some particular values are: $\gamma_{\alpha=0.25}^T = 2.51$; $\gamma_{\alpha=0.5}^T = 1.20$; $\gamma_{\alpha=0.75}^T = 0.77$; $\gamma_{\alpha=1}^T = 0.56$.

In Figure 8, we give some insight on the model in the case of a constant coupling parameter J. The results look similar to those displayed in Figures 6 and 7 excepted that the tricritical points depend on model parameters.

These results are consistent with those reported by Boukheddaden et al. [22] on the behavior of the critical temperatures T_M and T_c as functions of the magnetic coupling strength excepted that the form of the para-ferro transition line is quite different due to the thermal dependence of the interaction parameter K.

The transition lines divide the (T, γ) or (T, J) plane into three regions of stable phases as found in reference [22]. The dia-paramagnetic spin transition corresponding to T_{eq} is the only one transition in the model obtained at values of γ or J lower than a critical value γ_c or J_c where the second order transition line "diverges". At large values of γ or J, one obtains the full BEG model

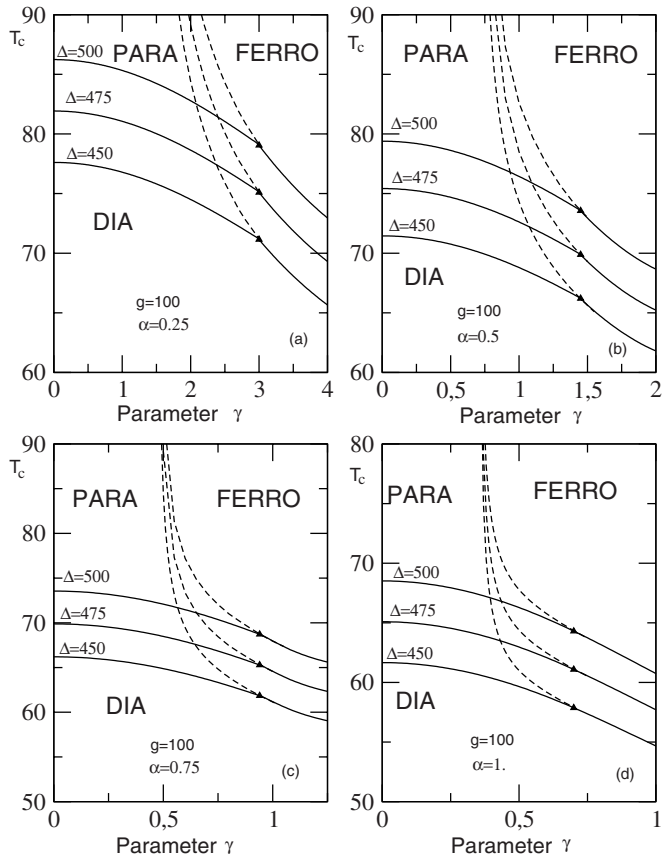

Fig. 7. Same captions as in Figure 6. Here, $g = 100$ and $\Delta = 500$ K. It is worthwhile to remark that Δ and g have no influence on the TCP.

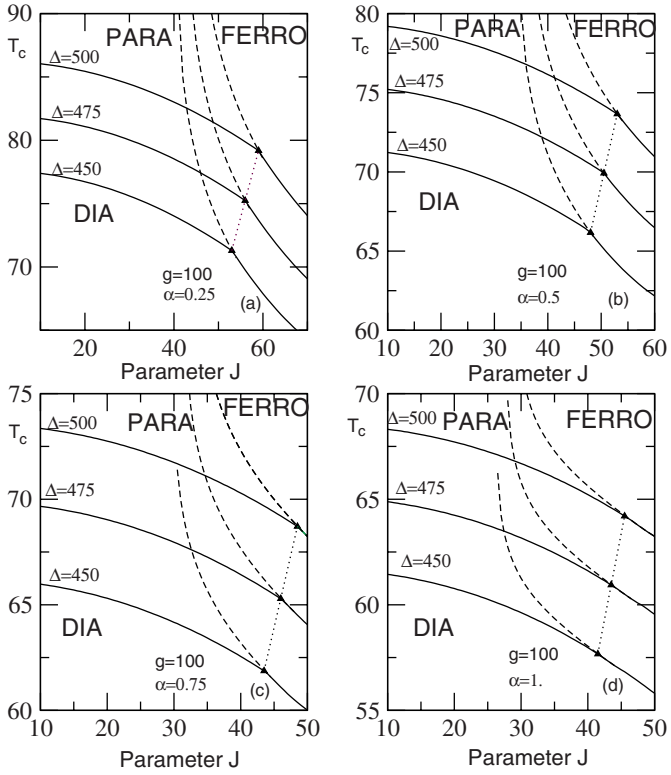

Fig. 8. Phase diagrams in general spin-crossover case where J is a varying constant. In this case, the tricritical lines are not vertical as in Figures 6 and 7.

which usually shows first and second order transitions. One can notice that when T_I denotes the second order transition temperature for $\gamma_c < \gamma \leq \gamma_\alpha^T$, $T_{eq} \leq T_I$ always and one assists to two transitions at fixed α when the temperature is raised. However, one does not encounter a reentrant ferromagnetic phase as in reference [22]. Instead, one has a reentrant paramagnetic phase in this range of γ values. Now, for $\gamma \geq \gamma_\alpha^T$, $T_c = T_{eq}$ when T_c denotes the first order transition temperature.

We have studied by simulations the non-equilibrium behavior of the system around the first-order transition T_c for $\gamma \neq 0$ or $J \neq 0$ using the same procedure as described above (Sect. 5.1). The running time is fixed to 10^4 s. Our calculations reveal that the magnetization m and the high spin fraction n_{HS} display the same trends. An increase of γ or J (at constant other parameters) increases the hysteresis loop's area and stabilizes the HS state. The same effect is observed when α increases at fixed γ or J.

We find instructive to check the behavior of the hysteresis loop in the static case where metastable states are long-lived by solving equations (14) by means of an iterative method. For this, we performed calculations by raising sequentially the temperature and then reducing it as described in Section 5.1 using a temperature step $\Delta T = 0.2$ K. We start from initial conditions $m = m_0$ and $q = q_0$ (initial state of the system) at temperature T; the system then converges to a fixed point with $m = m_1$ and $q = q_1$; at $T + \Delta T$, these values are used as new initial conditions and convergence leads to a new fixed point with $m = m_2$ and $q = q_2$ and so on. Here, we take J as a constant. Our calculations show that m and q display the same trends. The behaviors of n_{HS} and m are shown in Figure 9 for selected values of the model parameters. In Figures 9a and 9b, the coupling J is set to the value 0 which characterizes SC materials. Evidently, the magnetization $m = 0$ for both values of α. Comparing curves of Figures 4e and 9a obtained in almost the same conditions, one remarks that the hysteresis loop area or width is method-dependent. Indeed, the loop is almost absent in Figure 4e while here, it does exist. This result is not surprising since in KMC simulations, the hysteresis width also depends on duration time. What appears interesting is that the first-order transition temperatures derived from both methods (or figures) are almost the same. The width of the loop increases with increasing values of α (see Fig. 9b) as observed with KMC calculations and the transition is shifted to lower temperatures. In other panels of Figure 9, namely panels (c)–(f), usual values of Δ and g are considered. We get results that are in agreement with KMC findings. At fixed J, the hysteresis loop's width increases with increasing α as already found in panels (a) and (b). At fixed α, the width increases with J and the hysteresis loop is shifted to lower temperatures. Both order parameters display thermal hysteresis loops at the

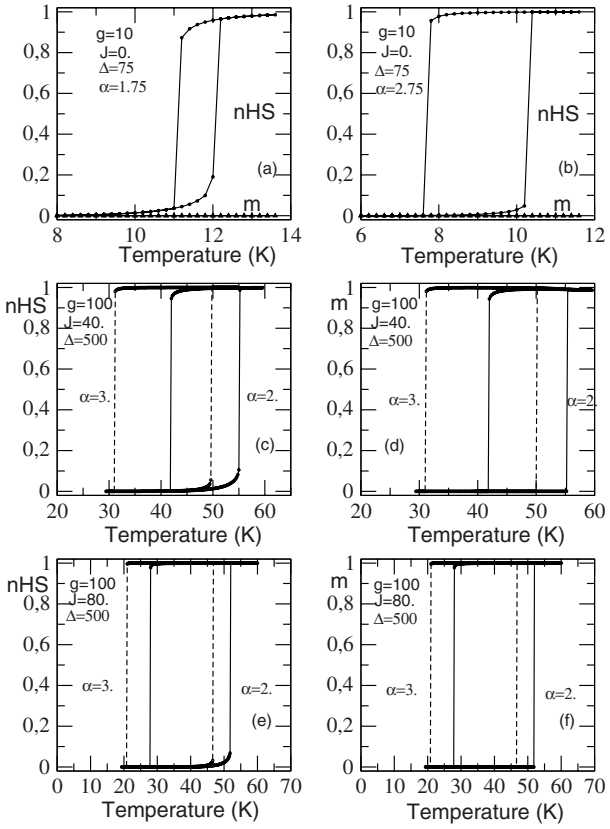

Fig. 9. Thermal static hysteresis loops of the HS fraction and the magnetization m calculated using the self-consistent equations (14). The values considered for the parameters are written in different panels. (a), (b) The magnetization $m = 0$ and the corresponding hysteresis is absent ($J = 0$). In other panels, the magnetization hysteresis loops and those for the HS fraction n_{HS} display similar trends for the same values of the model parameters.

vicinity of the first order transition temperature which also corresponds to the equilibrium temperature in this range of model parameters.

6 Conclusion

A common phenomenological description of SC and PBA materials that takes into account magnetic and elastic interactions has been reported in two dimensions by means of a BEG-type Hamiltonian with degenerate levels. The model has been investigated by two different methods: kinetic Monte Carlo simulations and corrective effective field calculations. Since symmetries associated to magnetic and spin-phonon interactions are different, two order parameters are considered to follow the SC transition. Results obtained by different methods show an impressive agreement. In the absence or at very weak magnetic interaction, the only one transition observed is the diamagnetic-paramagnetic transition. The latter is obtained when the proportion of spins in the HS and LS states are equal. This transition becomes of first order when the spin-phonon interaction becomes important. Otherwise a gradual conversion of spins from LS to HS states occurs when the temperature is raised from zero. The non-equilibrium hysteresis trend around the first order spin transition has been investigated and interesting behaviors have been also reported. In the presence of magnetic interaction, magnetic order and second order transition appear with the existence of a tricritical point which depends on model parameters. The finite-temperature phase diagrams reported on the model in this case display three different regions of stable phases: ferro, para and dia-magnetic phases. The results bear some resemblance with those reported some time ago by one the authors during an unifying description of the thermodynamical properties of spin-crossover materials [22]. They would be of great importance in the understanding of relaxation properties of excited magnetic state in PBA. An extention of this model to study the relaxation behavior of the photo-induced metastable HS fraction at low-temperature, using adapted Arrhenius rates is an interesting objective, since the competition beween magnetic and SC orders may lead to new self-organized magnetic structures.

The authors are indebted to Dr. Epiphane Codjovi who made this fruitfull collaboration possible. F.H. acknowledges financial support during a stay at ICTP (Trieste, Italy) where some of the calculations reported in this work have been performed.

Appendix A

In Hamiltonian (1), the degeneracy is a spectral property. In the following, we show that the difference in degeneracies of spin states enters calculations as a "field" term that depends linearly on temperature. Its relevant contribution is the ratio of degeneracies of spin states. Let us denote by g_0 the degeneracy of the $S = 0$ level and by $g_+ = g_-$ the degeneracy of the spin states $S = +1$ and $S = -1$ (degenerated in the abscence of exchange interaction). For N particles occupying these three levels, the total number of microstates is given by:

$$W(N_0, N_+, N_-) = \frac{N!}{N_0!N_+!N_-!} g_0^{N_0} g_+^{N_+} g_-^{N_-}$$

where $N = N_0 + N_+ + N_-$ with N_0 (N_+, N_-) denoting the respective number of particles in the spin state $S = 0$ ($S = +1$, $S = -1$). The occupation probability of the corresponding spin configuration with energy $E(N_0, N_+, N_-)$ follows:

$$P(N_0, N_+, N_-) \sim W(N_0, N_+, N_-) e^{-\beta E(N_0, N_+, N_-)};$$

$$P(N_0, N_+, N_-) \sim \frac{N!}{N_0!N_+!N_-!} \times e^{-\beta[E(N_0, N_+, N_-) - k_B T N_0 \ln(g_0) - k_B T (N_+ + N_-) \ln(g_+)]}.$$

Further calculations lead to the relation:

$$P(N_0, N_+, N_-) \sim \frac{N!}{N_0!N_+!N_-!} \times g_+^N e^{-\beta[E(N_0, N_+, N_-) - k_B T N_0 \ln(g)]},$$

where $g = g_+/g_0$ is the degeneracy ratio between HS and LS states.

Appendix B

Expressions of the coefficients $A_1(q)$, $A_2(q)$, $B_1(q)$, $B_2(q)$, $B_3(q)$, $C_1(q)$, $C_2(q)$ and $C_3(q)$ that are used to calculate the order parameters and correlation functions are:

$$\begin{aligned}
A_1(q) &= 4(1-\lambda)^3(1+3\lambda)[(1-q)^3K_3 \\
&\quad + 3(1-q)^2qK_2 + 3(1-q)q^2K_1] + q^3K_9] \\
&\quad + 6\lambda^2(1-\lambda)^2[(1-q)^2(2K_3+K_6) \\
&\quad + 2q(1-q)K_2 + 2q(K_4+K_5) \\
&\quad + q^2(K_{11}-2K_4-2K_5+2K_{12})] \\
&\quad + 4\lambda^3(1-\lambda)[(1-q)(K_3+K_7) \\
&\quad + q(K_{14}+K_{15}) + \lambda^4K_{16}], \\
A_2(q) &= 4(1-\lambda)^3(1+3\lambda)\,[(1-q)K_8 + qK_{10}] \\
&\quad + 6\lambda^2(1-\lambda)^2K_{13}, \\
B_1(q) &= (1-\lambda)^3(1+3\lambda)[(1-q)^4L_4 \\
&\quad + 4q(1-q)^3L_3 + 6(1-q)^2q^2L_2 + 4(1-q)q^3L_1 \\
&\quad + q^4L_{11}] + 6\lambda^2(1-\lambda)^2 \\
&\quad \times [(1-q)^3L_4 + 2q(1-q)^2L_3 + q^2(1-q)L_2 \\
&\quad + q(1-q)^2L_6 + 2q^2(1-q)L_5 + q^3L_{14}] \\
&\quad + 4\lambda^3(1-\lambda)[(1-q)^2L_4 \\
&\quad + q(1-q)L_3 + q(1-q)L_7 + q^2L_{17}] \\
&\quad + \lambda^4[(1-q)L_4 + qL_{19}], \\
B_2(q) &= 6(1-\lambda)^3(1+3\lambda)[(1-q)^2L_9 \\
&\quad + 2(1-q)qL_8 + q^2L_{12}] + 12\lambda^2(1-\lambda)^2 \\
&\quad \times [(1-q)L_9 + (1-q)L_{10} + q(L_{15}+L_{16})], \\
B_3(q) &= (1-\lambda)^3(1+3\lambda)L_{13}. \\
C_1(q) &= (1-\lambda)^2(1+2\lambda)[q(1-q)^3K_3 \\
&\quad + 3q^2(1-q)^2K_2 + 3q^3(1-q)K_1 + q^4K_9] \\
&\quad + 3\lambda^2(1-\lambda)^2[(1-q)^2qK_3 + (1-q)q^2K_4 \\
&\quad + q^2(1-q)K_{12} + q^2(1-q)K_2] \\
&\quad + \lambda^3(1-\lambda)[q(1-q)K_3 + q^2K_{15}] \\
&\quad + 3(1-\lambda)\lambda^3[q(1-q)K_7 + q^2K_{14}] + \lambda^4qK_{16}, \\
C_2(q) &= (1-\lambda)^2(1+2\lambda)[3q(1-q)K_8 \\
&\quad + 3q^2K_{10} + 3(1-q)^2K_2 + 6q(1-q)K_1 + 3q^2K_9] \\
&\quad + 3\lambda^2(1-\lambda)^2[qK_{13} + (1-q)K_5 \\
&\quad + qK_{11} + (1-q)K_2 + qK_{12}] + \lambda^3(1-\lambda)K_{14} \\
&\quad + 3(1-\lambda)\lambda^3K_{15}, \\
C_3(q) &= (1-\lambda)^2(1+2\lambda)K_{10}.
\end{aligned}$$

Appendix C

The coefficients K_i and L_i used in Appendix B are easily calculated using relation (14) and expressions of $f(x,y)$ and $g(x,y)$. Some examples are given below.

$$\begin{aligned}
K_1 &= e^{3K\nabla_y}\cosh^2(J\nabla_x)\sinh(J\nabla_x)f(x,y)_{/\substack{x=0\\y=0}} \\
K_6 &= e^{2K\nabla_y}\sinh(2J\nabla_x)f(x,y)_{/\substack{x=0\\y=0}} \\
K_{10} &= e^{4K\nabla_y}\cosh(J\nabla_x)\sinh^3(J\nabla_x)f(x,y)_{/\substack{x=0\\y=0}} \\
K_{16} &= e^{4K\nabla_y}\sinh(4J\nabla_x)f(x,y)_{/\substack{x=0\\y=0}} \\
L_1 &= e^{3K\nabla_y}\cosh^3(J\nabla_x)g(x,y)_{/\substack{x=0\\y=0}} \\
L_{10} &= e^{3K\nabla_y}\sinh(2J\nabla_x)\sinh(J\nabla_x)g(x,y)_{/\substack{x=0\\y=0}} \\
L_{13} &= e^{4K\nabla_y}\sinh^4(J\nabla_x)g(x,y)_{/\substack{x=0\\y=0}} \\
L_{19} &= e^{4K\nabla_y}\cosh(4J\nabla_x)g(x,y)_{/\substack{x=0\\y=0}}.
\end{aligned}$$

References

1. P. Gütlich, Struct. Bonding **44**, 83 (1981)
2. E. Konig, Struct. Bonding **76**, 51 (1991)
3. O. Kahn, Curr. Opin. Solid State Mater. Sci. **1**, 547 (1996)
4. S. Doniach, J. Chem. Phys. **68**, 4912 (1978)
5. A. Bousseksou, J. Nasser, J. Linares, K. Boukheddaden, F. Varret, J. Phys. I **2**, 1381 (1992)
6. A. Bousseksou, F. Varret, J. Nasser, J. Phys. I **3**, 1463 (1993)
7. A. Bousseksou, J. Constant-Machado, F. Varret, J. Phys. I **5**, 747 (1995)
8. R.R. Heikes, R.C. Miller, A. Mazelsky, Physica **30**, 1600 (1964)
9. G.H. Jonker, J. Appl. Phys. **37**, 1424 (1966)
10. K. Boukheddaden, J. Linarès, E. Codjovi, F. Varret, V. Niel, J.A. Real, J. Appl. Phys. **93**, 1 (2003)
11. L. Cambi, A. Gagnasso, Atti Accad. Naz. Lincei **13**, 809 (1931)
12. S. Decurtins, P. Gütlich, C.P. Köhler, H. Spiering, A. Hausser, Chem. Phys. Lett. **105**, 1 (1984)
13. J.J. McGarvey, I. Lawthers, J. Chem. Soc. Chem. Commun. **16**, 906 (1982)
14. F. Volatron, L. Catala, E. Rivière, A. Gloter, O. Stephan, T. Mallah, Inorg. Chem. **47**, 6584 (2008)
15. A. Muraoka, K. Boukheddaden, J. Linarès, F. Varret, Phys. Rev. B **84**, 054119 (2011)
16. A. Gîndulescu, A. Rotaru, J. Linares, M. Dimian, J. Naser, J. Phys.: Conf. Ser. **268**, 012007 (2011)
17. H. Tokoro, S.-I. Ohkoshi, K. Hashimoto, Appl. Phys. Lett. **82**, 1245 (2003)
18. F. Varret, K. Boukheddaden, C. Chong, A. Goujon, B. Gillon, J. Jeftic, A. Hausser, Eur. Phys. Lett. **77**, 30007 (2007)
19. J.A. Nasser, Eur. Phys. J. B **21**, 3 (2001)
20. K. Boukheddaden, S. Miyashita, M. Nishino, Phys. Rev. B **75**, 094112 (2007)
21. C. Enachescu, M. Nishino, S. Miyashita, A. Hausser, A. Stancu, L. Stoleriu, Eur. Phys. Lett. **91**, 27003 (2010)
22. K. Boukheddaden, M. Nishino, S. Miyashita, F. Varret, Phys. Rev. B **72**, 014467 (2005)

23. C. Enachescu, M. Nishino, S. Miyashita, A. Hauser, A. Stancu, L. Stoleriu, Eur. Phys. Lett. **91**, 27003 (2010)
24. H. Tokoro, S. Miyashita, K. Hashimoto, S. Ohkoshi, Phys. Rev. B **73**, 172415 (2006)
25. T. Kaneyoshi, I. Tamura, Phys. Rev. B **25**, 4679 (1982)
26. A.B. Bortz, M.H. Kalos, J.L. Lebowitz, J. Comp. Phys. **17**, 10 (1975)
27. S. Jain, *Monte Carlo simulations of disordered systems* (World scientific Publishing Co. Pte. Ltd, 1992)
28. R.J. Glauber, J. Math. Phys. **4**, 294 (1963)
29. J. Wajnflasz, Phys. Status Solidi B **40**, 537 (1970)
30. N. Goveas, G. Mukhopadhyay, Phys. Scr. **56**, 661 (1997)
31. J. Adler, Ph.D. thesis, University of New South wales, 1979 (unpublished)
32. M. Blume, V.J. Emery, R.B. Griffiths, Phys. Rev. A **4**, 1071 (1971)
33. J. Sivadiere, J. Lazerowitch, Phys. Rev. A **11**, 2079 (1975)
34. S.-I. Ohkshi, K. Imoto, Y. Tsunobuchi, S. Takano, H. Tokoro, Nat. Chem. **3**, 448 (2011)
35. M. Nakano, G. Matsubayashi, T. Matsuo, Phys. Rev. B **66**, 212412 (2002)
36. R. Honmura, Phys. Rev. B **30**, 348 (1984)
37. T. Kaneyoshi, Physica A **164**, 730 (1990)
38. T. Kaneyoshi, J.W. Tucker, M. Jascur, Physica A **186**, 495 (1992)
39. F. Zernike, Physica **7**, 565 (1940)
40. T. Kaneyoshi, Physica A **182**, 436 (1992)
41. Chin-Kun Hu, N.Sh. Izmailian, Phys. Rev. E **58**, 1644 (1998)
42. P.D. Beale, Phys. Rev. B **33**, 1717 (1986)
43. I. Shteto, K. Boukheddaden, F. Varret, Phys. Rev. E **60**, 5139 (1999)